Title

Label-free fluorescence lifetime spectroscopy detects radiation-induced necrotic changes in live brain in real-time.

Permalink

https://escholarship.org/uc/item/53d0r992

Journal

Biomedical Optics Express, 9(8)

ISSN

2156-7085

Authors

Hartl, Brad A
Ma, Htet SW
Sridharan, Shamira
et al.

Publication Date

2018-08-01

DOI

10.1364/boe.9.003559

Peer reviewed

Research Article Vol. 9, No. 8 | 1 Aug 2018 | BIOMEDICAL OPTICS EXPRESS 3559

Biomedical Optics EXPRESS

Label-free fluorescence lifetime spectroscopy detects radiation-induced necrotic changes in live brain in real-time

BRAD A. HARTL,[1] HTET S. W. MA,[1] SHAMIRA SRIDHARAN,[1] KATHERINE S. HANSEN,[2] MICHAEL S. KENT,[2] FREDRIC GORIN,[3] RUBEN C. FRAGOSO,[4] AND LAURA MARCU[1,*]

[1] *Department of Biomedical Engineering, University of California, Davis, CA 95616, USA*
[2] *Department of Surgical and Radiological Sciences, University of California Davis School of Veterinary Medicine, Davis, CA 95616, USA*
[3] *Department of Neurology, University of California Davis School of Medicine, Sacramento, CA 95817, USA*
[4] *Department of Radiation Oncology, University of California Davis School of Medicine, Sacramento, CA 95817, USA*
[*] *lmarcu@ucdavis.edu*

Abstract: Current clinical imaging modalities do not reliably identify brain tissue regions with necrosis following radiotherapy. This creates challenges for stereotaxic biopsies and surgical-decision making. Time-resolved fluorescence spectroscopy (TRFS) provides a means to rapidly identify necrotic tissue by its distinct autofluorescence signature resulting from tissue breakdown and altered metabolic profiles in regions with radiation damage. Studies conducted in a live animal model of radiation necrosis demonstrated that necrotic tissue is characterized by respective increases of 27% and 108% in average lifetime and redox ratio, when compared with healthy tissue. Moreover, radiation-damaged tissue not visible by MRI but confirmed by histopathology, was detected by TRFS. Current results demonstrate the ability of TRFS to identify radiation-damaged brain tissue in real-time and indicates its potential to assist with surgical guidance and MRI-guided biopsy procedures.

OCIS codes: (170.6280) Spectroscopy, fluorescence and luminescence; (300.2530) Fluorescence, laser-induced; (170.3650) Lifetime-based sensing; (170.4580) Optical diagnostics for medicine.

References and links

1. J. D. Ruben, M. Dally, M. Bailey, R. Smith, C. A. McLean, and P. Fedele, "Cerebral radiation necrosis: incidence, outcomes, and risk factors with emphasis on radiation parameters and chemotherapy," Int. J. Radiat. Oncol. Biol. Phys. **65**, 499–508 (2006).
2. P. Y. Wen and S. Kesari, "Malignant gliomas in adults," N. Engl. J. Med. **359**, 492–507 (2008).
3. F. G. Aksoy and M. H. Lev, "Dynamic contrast-enhanced brain perfusion imaging: technique and clinical applications," Semin. Ultrasound CT MR **21**, 462–477 (2000).
4. C. Asao, Y. Korogi, M. Kitajima, T. Hirai, Y. Baba, K. Makino, M. Kochi, S. Morishita, and Y. Yamashita, "Diffusion-weighted imaging of radiation-induced brain injury for differentiation from tumor recurrence," Am. J. Neuroradiol. **26**, 1455–1460 (2005).
5. E. E. Graves, S. J. Nelson, D. B. Vigneron, L. Verhey, M. McDermott, D. Larson, S. Chang, M. D. Prados, and W. P. Dillon, "Serial proton MR spectroscopic imaging of recurrent malignant gliomas after gamma knife radiosurgery," Am. J. Neuroradiol. **22**, 613–624 (2001).
6. F. Benard, J. Romsa, and R. Hustinx, "Imaging gliomas with positron emission tomography and single-photon emission computed tomography," Semin. Nucl. Med. **33**, 148–162 (2003).
7. D. D. Langleben and G. M. Segall, "PET in differentiation of recurrent brain tumor from radiation injury," J. Nucl. Med. **41**, 1861–1867 (2000).
8. T. Tihan, J. Barletta, I. Parney, K. Lamborn, P. K. Sneed, and S. Chang, "Prognostic value of detecting recurrent glioblastoma multiforme in surgical specimens from patients after radiotherapy: should pathology evaluation alter treatment decisions?" Hum. Pathol. **37**, 272–282 (2006).
9. P. A. Valdes, D. W. Roberts, F. K. Lu, and A. Golby, "Optical technologies for intraoperative neurosurgical guidance," Neurosurg. Focus **40**, E8 (2016).

#323491 https://doi.org/10.1364/BOE.9.003559
Journal © 2018 Received 20 Feb 2018; revised 28 Apr 2018; accepted 22 May 2018; published 5 Jul 2018

10. C. Fang, K. Wang, C. T. Zeng, C. W. Chi, W. T. Shang, J. Z. Ye, Y. M. Mao, Y. F. Fan, J. Yang, N. Xiang, N. Zeng, W. Zhu, C. H. Fang, and J. Tian, "Illuminating necrosis: From mechanistic exploration to preclinical application using fluorescence molecular imaging with indocyanine green," Sci. Rep. **6**, 21013 (2016).
11. J. Y. S. Lee and P. B. Little, "Studies of Autofluorescence in Experimentally Induced Cerebral Necrosis in Pigs," Vet. Pathol. **17**, 226–233 (1980).
12. E. E. Edwin and R. Jackman, "Nature of the autofluorescent material in cerebrocortical necrosis," J. Neurochem. **37**, 1054–1056 (1981).
13. R. Jackman and E. E. Edwin, "Cerebral Autofluorescence and Thiamine-Deficiency in Cerebrocortical Necrosis," Vet. Rec. **112**, 548–550 (1983).
14. T. Shibahara, R. Horino, T. Taniguchi, and Y. Ando, "Autofluorescent substance and neurocyte necrosis in thiamine deficiency in cattle," Aust. Vet. J. **77**, 329–330 (1999).
15. W. C. Lin, A. Mahadevan-Jansen, M. D. Johnson, R. J. Weil, and S. A. Toms, "In vivo optical spectroscopy detects radiation damage in brain tissue," Neurosurgery **57**, 518–525 (2005).
16. P. V. Butte, Q. Y. Fang, J. A. Jo, W. H. Yong, B. K. Pikul, K. L. Black, and L. Marcu, "Intraoperative delineation of primary brain tumors using time-resolved fluorescence spectroscopy," J. Biomed. Opt. **15**, 027008 (2010).
17. Y. H. Sun, N. Hatami, M. Yee, J. Phipps, D. S. Elson, F. Gorin, R. J. Schrot, and L. Marcu, "Fluorescence lifetime imaging microscopy for brain tumor image-guided surgery," J. Biomed. Opt. **15**, 056022 (2010).
18. P. V. Butte, A. N. Mamelak, M. Nuno, S. I. Bannykh, K. L. Black, and L. Marcu, "Fluorescence lifetime spectroscopy for guided therapy of brain tumors," Neuroimage **54**, S125–S135 (2011).
19. B. A. Hartl, H. S. W. Ma, K. S. Hansen, J. Perks, M. S. Kent, R. C. Fragoso, and L. Marcu, "The effect of radiation dose on the onset and progression of radiation-induced brain necrosis in the rat model," Int. J. Radiat. Biol. **93**, 676–682 (2017).
20. "American National Standard for Safe Use of Lasers in Health Care ANSI Z136.1," Laser Institute of America (2011).
21. D. L. Ma, J. Bec, D. Gorpas, D. Yankelevich, and L. Marcu, "Technique for real-time tissue characterization based on scanning multispectral fluorescence lifetime spectroscopy (ms-TRFS)," Biomed. Opt. Express **6**, 987–1002 (2015).
22. J. Liu, Y. Sun, J. Y. Qi, and L. Marcu, "A novel method for fast and robust estimation of fluorescence decay dynamics using constrained least-squares deconvolution with Laguerre expansion," Phys. Med. Biol. **57**, 843–865 (2012).
23. J. R. Lakowicz, *Principles of Fluorescence Spectroscopy* (Springer US, 2013).
24. F. Fereidouni, D. Gorpas, D. Ma, H. Fatakdawala, and L. Marcu, "Rapid fluorescence lifetime estimation with modified phasor approach and Laguerre deconvolution: a comparative study," Methods Appl. Fluoresc. **5**(3), 035003 (2017).
25. M. Morawski, G. Bruckner, T. Arendt, and R. T. Matthews, "Aggrecan: Beyond cartilage and into the brain," Int. J. Biochem. Cell Biol. **44**, 690–693 (2012).
26. J. C. F. Kwok, P. Warren, and J. W. Fawcett, "Chondroitin sulfate: A key molecule in the brain matrix," Int. J. Biochem. Cell Biol. **44**, 582–586 (2012).
27. I. Bjorkhem and S. Meaney, "Brain cholesterol: Long secret life behind a barrier," Arterioscl. Throm. Vas. **24**, 806–815 (2004).
28. J. Cohen, *Statistical Power Analysis for the Behavioral Sciences* (Taylor & Francis, 2013).
29. Gail M. Sullivan and Richard Feinn, "Using Effect Size-or Why the P Value Is Not Enough," J. Grad. Med. Educ. **4**, 279–282 (2012).
30. R. G. Brereton, *Chemometrics: Data Analysis for the Laboratory and Chemical Plant* (Wiley, 2003).
31. X. Y. Jiang, L. Y. Yuan, J. A. Engelbach, J. Cates, C. J. Perez-Torres, F. Gao, D. Thotala, R. E. Drzymala, R. E. Schmidt, K. M. Rich, D. E. Hallahan, J. J. H. Ackerman, and J. R. Garbow, "A Gamma-Knife-Enabled Mouse Model of Cerebral Single-Hemisphere Delayed Radiation Necrosis," Plos One **10**, e0139596 (2015).
32. C. Abram, M. Pougin, and F. Beyrau, "Temperature field measurements in liquids using ZnO thermographic phosphor tracer particles," Exp. Fluids **57**, 115 (2016).
33. D. Greene-Schloesser, M. E. Robbins, A. M. Peiffer, E. G. Shaw, K. T. Wheeler, and M. D. Chan, "Radiation-induced brain injury: A review," Front. Oncol. **2**, 73 (2012).
34. M. C. Skala, K. M. Riching, A. Gendron-Fitzpatrick, J. Eickhoff, K. W. Eliceiri, J. G. White, and N. Ramanujam, "In vivo multiphoton microscopy of NADH and FAD redox states, fluorescence lifetimes, and cellular morphology in precancerous epithelia," P. Natl. Acad. Sci. **104**, 19494–19499 (2007).
35. T. S. Blacker and M. R. Duchen, "Investigating mitochondrial redox state using NADH and NADPH autofluorescence," Free Radical Bio. Med. **100**, 53–65 (2016).
36. T. S. Blacker, Z. F. Mann, J. E. Gale, M. Ziegler, A. J. Bain, G. Szabadkai, and M. R. Duchen, "Separating NADH and NADPH fluorescence in live cells and tissues using FLIM," Nat. Commun. **5**, 3936 (2014).
37. W. Ying, "NAD+/NADH and NADP+/NADPH in cellular functions and cell death: regulation and biological consequences," Antioxid. Redox Signal. **10**, 179–206 (2008).
38. M. A. Yaseen, J. Sutin, W. Wu, B. Fu, H. Uhlirova, A. Devor, D. A. Boas, and S. Sakadžić, "Fluorescence lifetime microscopy of NADH distinguishes alterations in cerebral metabolism in vivo," Biomed. Opt. Express **8**, 2368–2385 (2017).
39. K. Blinova, R. L. Levine, E. S. Boja, G. L. Griffiths, Z. D. Shi, B. Ruddy, and R. S. Balaban, "Mitochondrial NADH fluorescence is enhanced by Complex I binding," Biochem. **47**, 9636–9645 (2008).
40. B. Valeur and M. N. Berberan-Santos, *Molecular Fluorescence: Principles and Applications* (Wiley, 2013).

41. A. Gafni and L. Brand, "Fluorescence Decay Studies of Reduced Nicotinamide Adenine-Dinucleotide in Solution and Bound to Liver Alcohol-Dehydrogenase," Biochem. **15**, 3165–3171 (1976).
42. W. Zheng, Y. Wu, D. Li, and J. Y. Qu, "Autofluorescence of epithelial tissue: single-photon versus two-photon excitation," J. Biomed. Opt. **13**, 054010 (2008).
43. M. A. Yaseen, S. Sakadzic, W. Wu, W. Becker, K. A. Kasischke, and D. A. Boas, "In vivo imaging of cerebral energy metabolism with two-photon fluorescence lifetime microscopy of NADH," Biomed. Opt. Express **4**, 307–321 (2013).
44. J. Vergen, C. Hecht, L. V. Zholudeva, M. M. Marquardt, R. Hallworth, and M. G. Nichols, "Metabolic Imaging Using Two-Photon Excited NADH Intensity and Fluorescence Lifetime Imaging," Microsc. Microanal. **18**, 761–770 (2012).
45. F. S. Pavone, and S. Shoham, "Label-free fluorescence interrogation of brain tumors," in *Handbook of Neurophotonics* (CRC Press Taylor & Francis, 2018).

1. Introduction

Radiation-induced brain necrosis is a complication of radiation therapy (RT) which presents as an irreversible, progressive necrotic lesion within a few weeks after initial treatment, or can appear years after the initial treatment [1]. Due to the variable timeline of presentation and overlap of symptoms with tumor recurrence, differential diagnosis of radiation-induced necrosis and tumor recurrence can be challenging [2]. Accurate and timely diagnosis is a critical determinant of patient outcome because different clinical management strategies are adopted for each condition–notably, a much more aggressive plan of action for tumor recurrence [2].

Delineation of radiation-induced necrosis in the brain has been attempted with a variety of preoperative imaging modalities, but with limited success. Magnetic resonance imaging (MRI) has produced varied results in identifying radiation-induced necrosis and recurrent tumor margins [3, 4]. Proton magnetic resonance spectroscopy has also been evaluated, however, studies conducted so far have shown mixed results, suggesting that supplementary means are still necessary [5]. Single-photon emission computed tomography (SPECT) has good specificity for diagnosis, but suffers from poor resolution [6]. Positron emission tomography has improved resolution but less specificity compared to SPECT [7]. While these imaging modalities show promise, pathological assessment of biopsied tissue obtained during invasive and time-intensive surgery or stereotaxic biopsy is still the clinical gold standard [8].

A variety of optical techniques have been investigated for differentiating tumor from healthy brain regions and as a means of 'optical biopsy' in situ [9]. However, only a limited number of studies have investigated the properties of necrotic tissues in the brain, none of which have measured the optical scattering or absorption coefficients. The fluorescence from indocyanine green, as well as from endogenous fluorophores, has been investigated for detecting thermally-induced brain necrosis in animals [10, 11]. Autofluorescence of brain necrotic regions has also been observed in bovine subjects with cerebrocortical necrosis [12-14]. Only one study reported on a unique autofluorescence spectral feature of radiation-induced brain necrosis in humans, but did not explore the contrast mechanisms behind the signals observed [15].

Time-resolved fluorescence spectroscopy (TRFS) employed herein is an autofluorescence-based lifetime measurement technique that provides robust information about endogenous fluorophores present in tissue. The primary contributors to the fluorescence emission spectra in the brain are nicotinamide adenine dinucleotide (phosphate) (NAD(P)H) and flavin adenine dinucleotide (FAD), which have diverse signatures based upon a tissue's metabolic state. TRFS also measures the fluorescence from extracellular matrix (ECM) elements. Previously, we used such signatures to discriminate between white and gray matter, as well as brain tumor tissues, intra-operatively [16-18]. Thus, TRFS is well suited to assess both metabolic changes and structural breakdown in tissue, and therefore differentiate radiation-induced necrosis from healthy brain tissue.

In this study, we demonstrate a) the TRFS technique as a means to elucidate the contrast mechanisms behind necrotic tissue autofluorescence properties associated with the breakdown of tissue structure and shifts in metabolite populations, b) the ability of this optical technique for real-time detection of necrotic changes in live brain indicating the TRFS's potential to inform surgical decision making, and c) the use of *in vitro* studies mimicking necrotic cell death to enhance our understanding of the relationship between fluorescence lifetime signatures and different forms of cell death. Two TRFS instrumental setups were employed in the study. A high spectral resolution point-TRFS (p-TRFS) was used to study the biological sources of autofluorescence in radiation-induced brain necrosis while a fast multispectral-TRFS (ms-TRFS) system was used to demonstrate the ability of this technique to assess and display in real-time during clinically relevant situations (craniotomy and stereotaxic biopsy) the optical data that encode the metabolic features of different brain tissue types.

It is well known that the *ex vivo* autofluorescence signature from brain tissue is significantly different than *in vivo* [16]. To measure the brain tissue in an unperturbed state, studies were performed using a unique rat model of radiation necrosis with an optical fiber progressively inserted into the tissue. The animal model allowed for the assessment of histopathologically non-viable necrotic tissue as well as of metabolic changes prior to the formation of necrosis (pre-necrosis) in still viable tissue. The collective results from these studies provide critical insight into the mechanism of contrast from endogenous NAD(P)H and FAD fluorescence in necrotic brain tissue and show the TRFS's ability to resolve radiation-induced necrosis in live brain including necrotic changes not visible by MRI.

2. Methods

2.1. Animal model and irradiation

Brain necrosis was induced with a single-fraction of 6 MV photon radiation to the right hemisphere of eight-week-old male Fischer CDF rats (Charles River Laboratories) using a linear accelerator (LINAC) (TrueBeam, Varian Medical Systems). The radiation dose plan (Fig. 1(A)), as reported in greater detail previously [19], was adjusted so that the contralateral hemisphere would receive less than 10 Gray (Gy) for a targeted 60-Gy (point maximum) dose on the right hemisphere. A 1-cm-thick bolus (Superflab, Radiation Products Design, Inc.) was placed atop of the animal's head during the irradiation to bring more of the targeted dose up and into the brain parenchyma. This dose plan has been shown to be well tolerated by the animals, with the first signs of necrosis consistently occurring at ~17 weeks after irradiation [19]. Animals were randomly assigned to study groups and irradiated in groups of 6 or fewer per week to accommodate the scheduling of the LINAC, MRI, and surgeries. All procedures described were approved by the University of California, Davis Institutional Animal Care and Use Committee (protocol 18317).

2.2. Pre-operative MR imaging

All animals received a preoperative MRI, as previously described [19], on the day before surgery to noninvasively assess the presence or absence of necrosis. Briefly, T2-weighted images (TR = 6100 ms, TE = 60 ms, 0.5 mm slice thickness, 0.5 mm slice spacing, 44 slices total, 3×2 cm^2 field of view, 125×125 µm^2 pixel resolution) were acquired on a BioSpec 7T (Bruker Corporation) at the Center for Molecular and Genomic Imaging (University of California, Davis).

2.3. Surgical procedure for TRFS measurements

The brain tissue of the rats was assessed via a terminal surgical procedure either one week prior to the onset of necrosis (pre-necrosis groups; n = 8 treated, n = 5 control) or at the approximate maximum volume of necrosis formation (necrosis groups; n = 9 treated, n = 9 control). To account for aging, control groups of animals were assessed with surgery for each of these two time-points. The rats were anesthetized using isoflurane (induction at 2-3%, maintenance at 1-2%) and placed into a small-animal stereotaxic frame equipped with a nose cone and warming bed with active feedback to maintain body constant body temperature. Rodents received 3.0 mL saline subcutaneous injections to prevent dehydration. An incision was made with a scalpel to

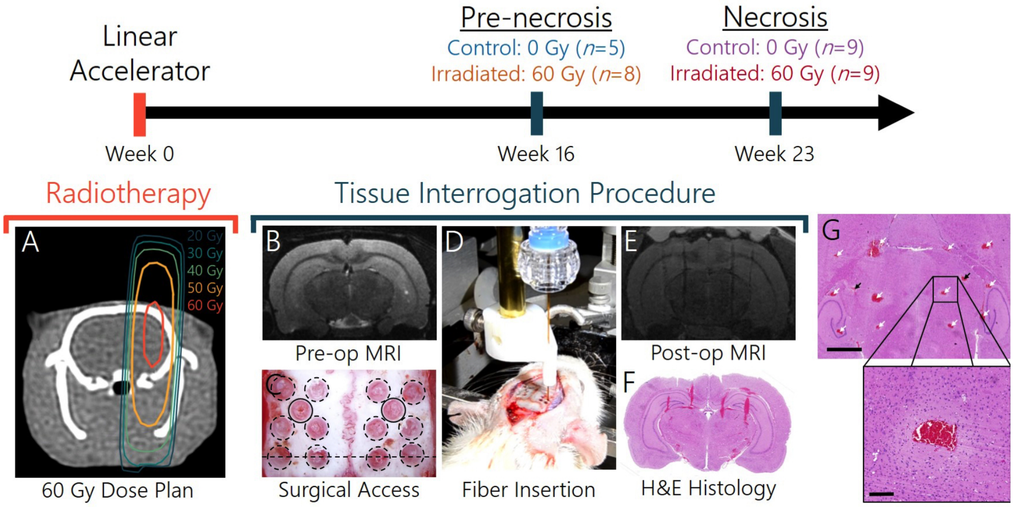

Fig. 1. Timeline and overview of in vivo experimental methods; n indicates number of animals per group. (A) Radiation dose plan overlaid onto axial CT scan with the animal placed in prone position; 20-, 30-, 40-, 50-, 60-Gy isodose lines are shown. A 1-cm-bolus (not shown) was placed on the rat's head to maximize isodose coverage in the brain. (B) Preoperative axial T2-weighted MRI used for surgical planning. (C) Overhead image of the burr hole pattern on top of rat skull corresponding to where vertical depth scans with TRFS were performed. The central hole on each hemisphere, indicated by solid-lined black circles, is where p-TRFS scans were performed (dash-lined circles for ms-TRFS) and the dashed black horizontal line denotes the scan plane location of B, E, and F. (D) Assessment of brain tissue during live surgery where the fiber was stereotaxically inserted and progressed with a custom-built motorized fiber holder. (E) Postoperative axial T2-weighted MRI showing the needle track locations. (F) Corresponding H&E stained histology section of the same region as B and E, also showing the presence of needle tracks. (G) Histology at 5 mm below the dorsal surface of the brain with ms-TRFS and p-TRFS needle tracks denoted with white and black arrows, respectively. Inset shows zoomed in image for a single ms-TRFS needle track (scale bars are 2.0 and 0.2 mm). The lateral bounds of tissue damage, observed as reduced pigmentation around each needle track, is well contained and not extending to adjacent tracks.

expose the skull from coronal to lambdoid sutures and the periosteum layer was removed. An array of burr holes was used instead of a craniotomy to access the brain tissue to prevent brain swelling and provide more robust fiducial landmarks for data coregistration. MRI scans were assessed to identify the location of necrosis for burr hole placement (see Fig. 1(B) and 1(E)). The hole used for p-TRFS measurements (Fig. 1(C)) was placed approximately at the center of the necrosis, corresponding to 3.5 mm lateral and 3.5 mm posterior relative to bregma. Six additional burr holes were created on the irradiated side of the skull to interrogate the tissue with ms-TRFS measurements. An additional set of seven burr holes were also created on the non-irradiated side of the brain in an identical pattern to provide internal control measurements. Burr holes were made under a microscope using a 1.6 mm diameter spherical burr bit driven by a high-speed rotary tool and were created to expose–but not disrupt–the dura matter. Saline was externally applied to the brain surface to keep the bone and brain tissue hydrated during the procedure and to reduce local hyperthermia caused by the drilling. When major pial vessels were present, holes were expanded or shifted so that vessels wouldn't be disrupted.

2.4. p-TRFS instrumentation and data acquisition

The excitation source for the p-TRFS system was a pulsed (0.97 µJ/pulse) 355 nm laser (STV-02E-140, Teem Photonics). A 600 µm core diameter optical fiber (FVP600660710, Molex) with a 45° polished tip was used to excite and collect the emission. Fluorescence emission was selected with a monochromator (MicroHR, Horiba), measured with a gated microchannel plate photomultiplier tube (R5916U-50, Hamamatsu) connected to a high-speed amplifier (C5594, Hamamatsu), and digitized by an oscilloscope (DPO7254, Tektronix). To reduce tissue exposure and comply with ANSI radiation exposure limits [20], a beam shutter (SHB05T, Thorlabs) was used to block the laser light while the monochromator changed wavelengths. Fluorescence decays were acquired at 0.05 ns resolution and averaged 64 times for wavelengths between 375 and 600 nm (5 nm increments). Since p-TRFS measurements account for the full spectral emission, it is well suited for characterization of the sources of optical contrast in tissue. However, it takes ~45 s to acquire data at each point, limiting its applicability for real-time diagnosis.

The optical fiber was attached to a stereotaxic arm using a needle holder, and measurements were acquired from 1.0 to 10.0 mm below the surface (1.0 mm intervals, 18 scans per animal). To ensure that the tissue being measured was as unperturbed as possible, data was acquired only as the needle was advanced into the tissue, and never upon retraction to prevent any interference from bleeding. The tip of the optical fiber was wiped clean before insertion into each burr hole. Software written in LabVIEW (National Instruments) was used to control and automate all peripherals and data acquisition. The set-up and acquisition of p-TRFS data required ~25 min and followed immediately after surgical preparation was complete.

2.5. ms-TRFS Instrumentation and data acquisition

The ms-TRFS system has been described previously [21], the key specifications and modifications are included herein. The excitation source and optical fiber were the same as for the p-TRFS except that the energy per pulse was 0.92 µJ and a 400 µm core diameter fiber was used (FVP400440480, Molex). The bandpass filters used in the wavelength selection module had center wavelengths/bandwidths of 390/40, 470/28, and 540/50 nm (FF01-390/40-25, FF01-470/28-25, FF01-540/50-25, Semrock); corresponding to the emission of ECM proteins, NAD(P)H, and FAD, respectively. For these acquisitions, the fluorescence was measured using a microchannel plate photomultiplier tube (R3809U-50, Hamamatsu) and amplified using a high frequency amplifier (AM-1607-3000, L-3 Narda-MITEQ). Fluorescence decays were acquired at 0.08 ns resolution and averaged 16 times using a digitizer (PXIe-1082, National Instruments). ms-TRFS measurements are rapid and can be acquired at the rate of 5 points/s. Therefore, the ms-TRFS technique is better suited for real-time tissue diagnostics.

For the ms-TRFS measurements, the optical fiber was mounted into a custom-built motorized fiber holder attached to the stereotaxic arm (Fig. 1(D)). Similar to the p-TRFS system, data was acquired during fiber descent and LabVIEW software was used for instrument control and acquisition. The optical fiber was advanced into the tissue at 0.2 mm/s to depths up to 10 mm, yielding approximately 200 measurements per depth scan. The tip of the optical fiber was wiped clean before insertion into each burr hole. The setup and acquisition of ms-TRFS required ~25 min and followed immediately after p-TRFS measurements were complete; the entire surgical procedure lasted approximately two hours.

2.6. TRFS data processing

Analysis and processing of the fluorescence lifetime data was performed using a constrained least-squares deconvolution method based on Laguerre basis expansion [22], which provides a rapid means to retrieve the average lifetime and is suitable for clinical implementation. Notably, the decays were expanded upon 12 ordered Laguerre basis functions using constant alpha value parameters for each of the data sets. The average fluorescence lifetime, τ_{avg}, was calculated as follows where $\hat{h}(i)$ is the estimated deconvolved fluorescence intensity decay for N acquired time-points at the sampling interval δt [23]

$$\hat{\tau}_{avg} = \frac{\delta t \sum_{i=0}^{N-1} i\hat{h}(i)}{\sum_{i=0}^{N-1} \hat{h}(i)}. \tag{1}$$

Temporal phasor analysis was performed as an additional means for rapid analysis of the decays. Briefly, this entails calculating the Fourier transform of the decay curve and has been previously described elsewhere [24]. Phasor analysis was exclusively used for the support vector machine (SVM)-based classifier as opposed to direct analysis of the different tissue types.

The decays from p-TRFS were also fit to a more computationally expensive biexponential model using non-linear least-squares to assess the complex decay profile of the multiple fluorophores and species found in tissue, notably the bound and unbound forms of NAD(P)H and FAD [23]. The biexponential model is represented as the intensity summation of decay components,

$$I(t) = \alpha_1 e^{(-t/\tau_1)} + \alpha_2 e^{(-t/\tau_2)}, \tag{2}$$

where α_1 and α_2 are the pre-exponential factors, and τ_1 and τ_2 the decay time constants for each of the components [23]. The contribution from each component to the overall decay is represented as

$$\beta_l = \frac{\alpha_l \tau_l}{\alpha_1\tau_1 + \alpha_2\tau_2}, \tag{3}$$

corresponding to an average lifetime of

$$\tau_{avg} = \beta_1\tau_1 + \beta_2\tau_2. \tag{4}$$

The biexponential model was used over higher orders as it was found to provide the best fit, with higher orders often converging down to a biexponential solution. The calculated redox ratio for p-TRFS and ms-TRFS data is defined as

$$\text{redox ratio} \approx \frac{Int_{600}}{Int_{465}} \approx \frac{Int_{Ch.3}}{Int_{Ch.2}}, \tag{5}$$

where Int_{600} and Int_{465} are the fluorescence intensities at 600 and 465 nm, respectively for the p-TRFS measurements; and Int_{Ch3} and Int_{Ch2} are the fluorescence intensities for channels 3 and 2, respectively for the ms-TRFS measurements. The wavelengths were chosen to provide the intensities with the largest contribution from FAD (600 nm, channel 3) and NAD(P)H (465 nm, channel 2), relative to the other fluorophore. Spectral contribution analysis was performed by fitting the tissue spectra to a summation of spectra from NAD(P)H, FAD, aggrecan, chondroitin sulfate, and cholesterol (Sigma-Aldrich), all of which are known to be present in healthy brain tissue [23, 25-27]. Since the ECM molecules aggrecan and chondroitin sulfate, and cholesterol have similar emission spectra, they were grouped together to avoid overfitting of the data. Unbound NADH and NADPH were also grouped together due to their nearly identical fluorescence spectral and lifetime characteristics. The relative contributions from each of the components were determined using a nonnegative least-squares fitting in MATLAB.

2.7. Methodological validation of ms-TRFS using p-TRFS

To allow for a direct comparison of the two TRFS systems, the p-TRFS measurements were converted to the three channels of the ms-TRFS system as follows for intensity and average lifetime, respectively,

$$Int_{Ch.j} = \sum_{k=\lambda_1}^{\lambda_2} Int_k \tag{6}$$

and

$$\tau_{Ch.j} = \frac{\sum_{k=\lambda_1}^{\lambda_2} \tau_k Int_k}{\sum_{k=\lambda_1}^{\lambda_2} Int_k} \tag{7}$$

Where λ_1 and λ_2 are the lower and upper wavelength bounds of the j^{th} channel, and Int_k and k are the intensities and average lifetimes of the k^{th} wavelength of the p-TRFS spectra.

In the brain, the most significant spectral differences in healthy and necrotic tissue are observed in the NAD(P)H and FAD spectra. In the ms-TRFS system, channel 2 has been optimized for NAD(P)H spectral emission bands at 456-484 nm and channel 3 has been optimized for FAD spectra at 515-565 nm emission bands. Figure 2 shows the comparison of ms-TRFS data in channels 2 and 3, and data from corresponding bands in p-TRFS. The average difference in the two channels for lifetime was only 0.03 ns and 0.04 ns for the control healthy pre-necrotic and necrotic tissues, respectively, but was significantly larger for the irradiated pre-necrotic and necrotic tissues, both at 0.12 ns. This small discrepancy is likely due to the biological variations in the physical brain locations sampled by the two imaging modalities (See Fig. 1(C): Surgical Access for a visual representation of physical regions measured). It is possible that p-TRFS sampled more advanced and hypoxic regions within the necrotic center based on the location of the burr hole relative to the location where the radiation treatment was focused. In the stratified histology grading analysis, average lifetimes were found to correlate with the severity of the necrotic tissue, thus supporting this locational discrepancy hypothesis. Thus, the true sensitivity and specificity for detecting necrosis using the automated SVM classifier in the brain using ms-TRFS (see Table 1) likely lies somewhere between the reported values for ms-TRFS and the p-TRFS converted to ms-TRFS.

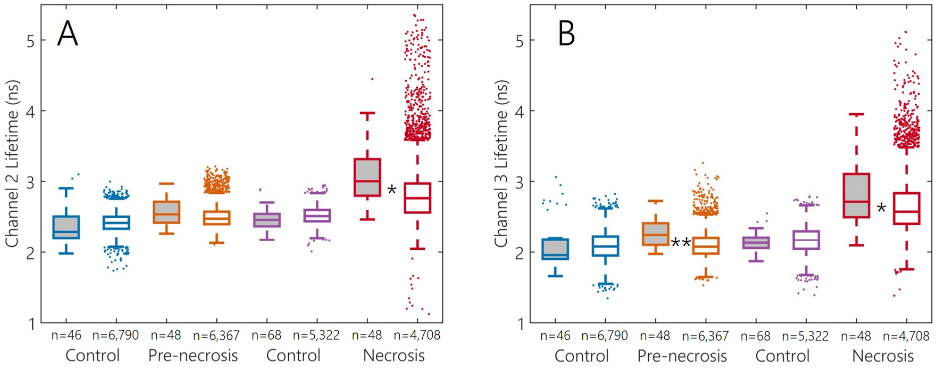

Fig. 2. Fluorescence lifetimes from both the p-TRFS and ms-TRFS measurements are in good agreement. Channel 2 (A) and channel 3 (B) average lifetimes from the p-TRFS (grayed boxes) and ms-TRFS (white boxes) measurements are shown. The values for p-TRFS points were calculated using intensity weighted averages of the average lifetimes at individual wavelengths corresponding to the ms-TRFS channel windows (see Fig. 4(A)-(B)). Values shown are mean ± SD; * ES > 0.5 and ** ES > 0.8.

2.8. *Multi-modal data coregistration*

Upon completion of the *in vivo* TRFS measurements, animals were transcardially perfused with PBS and then 10% formalin. The decapitated head was rescanned with MRI 0-3 days after surgery to track the locations assessed with the fiber-optic probe. Brains were then extracted from the skulls and sliced using a custom-built brain matrix to expose the brain's dorsal side and allowing for precise 1 mm axial sections to be cut. Representative slices were collected for the four rows of needle tracks, embedded in paraffin, sectioned and stained with hematoxylin and eosin (H&E). The needle tracks corresponding to the fluorescence measurements were easily detected in the postoperative MRI images (Fig. 1(E)) and were coregistered to the preoperative MRI images using fiducial landmarks from the intact skulls present in both image sets. The regions along each needle track were then segmented into healthy, necrosis, or a mixture of these two tissue types based on the preoperative MRI scans and H&E histology images. Regions were classified as necrosis when tissue loss and/or edema were present. As no standard exists for detecting pre-necrosis, it was defined as regions where necrosis was observed in at least 75% of the necrosis animals. The top one millimeter of tissue below the surface was often found to have significant contributions from bone collagen, which was due to a variety of factors but mostly attributed to the probe not always immediately puncturing through the dura. These areas were excluded from analysis, along with regions where contamination from bone or the ventricles (as annotated in Fig. 3(A)) occurred.

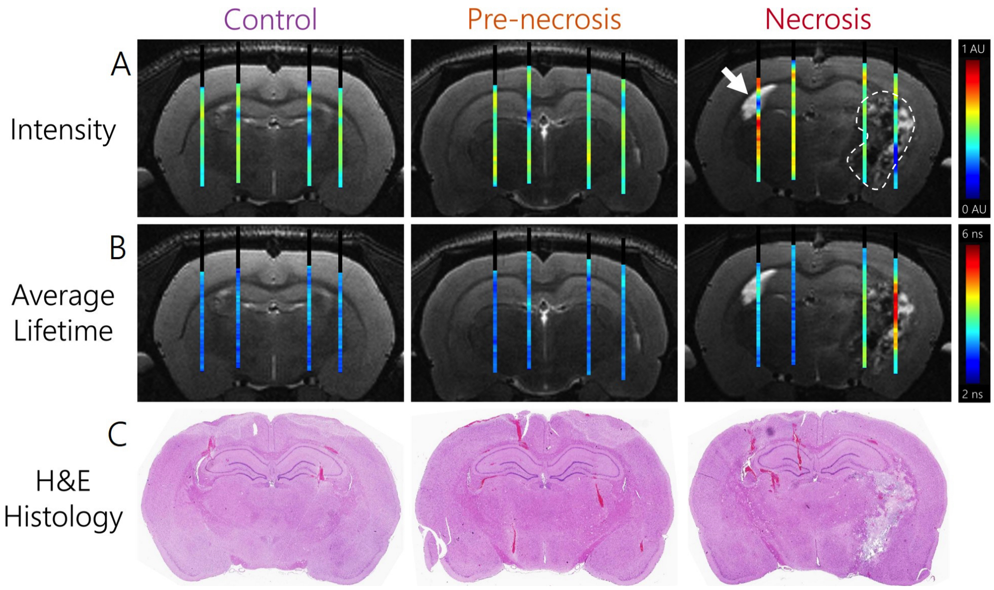

Fig. 3. Fluorescence intensities and average lifetimes from ms-TRFS measurements correspond to features observed in T2-weighted MRI scans and H&E stained histology. Representative preoperative MRI scans with ms-TRFS channel 2 fluorescence intensity (A) and average lifetime (B) measurements overlaid; corresponding H&E stained histology are shown below (C). The left ventricle has been marked with a white arrow on the necrosis MRI image and the approximate regions of necrosis have been indicated with a dashed line.

2.9. *Statistical analysis and supervised machine learning*

Statistical analysis was performed using a mixed-effects model to account for the hierarchical nature of the repeated measurements over time within subject as well as baseline covariates. The

Tukey's multiple-comparison procedure was applied to determine significance (*p*-values) for each fluorescence lifetime parameter comparing the different tissue types. In addition, receiver operating characteristic (ROC) curves were used to further refine the most informative variables to discriminate the different tissue types. For each of the TRFS parameters the area under the curve (AUC) and Cohen's *d* [28] effect size (ES) were calculated to estimate discriminating power when comparing each of the different tissue types. Further classification analysis was carried out with the supervised learning model SVM. To reduce potential overfitting of the data and compensate for the high sample size on the effect of the *p*-values [29], only a subset of the parameters with *p*-values less than 0.001 and AUC greater than 0.9 were used to train the SVM algorithm. To avoid over fitting, a leave-one-out cross-validation (LOOCV) protocol was then used to determine the sensitivity (SN), specificity (SP), positive predictive value (PPV), and negative predictive value (NPV) of the fluorescence lifetime spectroscopy parameters to differentiate the different tissue types [30].

2.10. *In vitro studies*

F98 cells (American Type Culture Collection) were cultured in monolayers at 37 C and 5% CO_2 in Dulbecco's Modified Eagle Medium (Gibco) without phenol red indicator and with 10% fetal bovine serum, penicillin (100 U/ml) and streptomycin (100 µg/ml). The F98 glioma cell line was chosen because it was derived from the same inbred Fischer rat strain used for the *in vivo* studies. Although performing these studies with cultured native glial and neural cells could be potentially more representative of the brain parenchyma, such a complicated study is well beyond the scope of the current work. Cells were trypsinized, washed with phosphate buffered saline (PBS), and then treated with either sodium azide for 5 min or saponin for 30 min. Sodium azide was used at 50 mM (102891, MP Biomedicals) and saponin at 0.1% w/v (102855, MP Biomedicals). Due to the variety of fluorophores and chromophores present in complete media, cells were washed and suspended in PBS following the drug treatment for p-TRFS measurements. After completion of the cell suspension studies, cell viabilities of the different treatment types were assessed with the colony formation assay. Experiments were repeated three times.

3. Results

3.1. *Tissue autofluorescence assessment with p-TRFS*

The endogenous fluorophores present in different types of brain tissue, necrotic and healthy, were evaluated using high spectral resolution p-TRFS in a previously described rat model of radiation necrosis [19] (Fig. 1). The animals that developed necrosis were a few weeks older than animals in the pre-necrosis groups. To account for changes due to necrosis progression within the context of aging, animals in each treatment group had age-matched controls. Necrotic tissue displayed higher intensities at all wavelengths above 465 nm ($P < 0.001$) and lower intensities in the shorter wavelengths of 400-420 nm in comparison to healthy controls ($P < 0.001$) (Fig. 4(A)). Minimal changes were observed in the pre-necrotic tissue (Fig. 4(A)). No significant change in peak position was observed for either diseased tissue types, suggesting that no additional fluorophores are generated during necrosis progression. Statistically significant increases in average lifetime, calculated using Laguerre expansion, were observed for both pre-necrotic ($P < 0.05$) and necrotic ($P < 0.001$) tissues relative to their respective age-matched controls at the 410-550 nm emission wavelength band (Fig. 4(B)). A consistent decrease in average lifetime was observed with increasing wavelengths in all diseased and healthy tissue. Representative H&E stained histology, as well as T2-weighted MRI scans, from each of the different tissue types are shown for reference in Fig. 4(C)-(D). Large increases were also present in the full width at 70% of maximum in the fluorescence intensity spectrum ($P < 0.001$) (Fig. 4(E)) and redox ratio ($P < 0.001$) (Fig. 4(F)) of necrotic tissue, although minimal changes were observed in pre-necrotic tissue. The most pronounced spectral changes were observed in necrotic tissue in regions of significant tissue loss and edema, as assessed from coregistration of p-TRFS data with histology images. There was limited fluorescence below 415 nm and interference from Raman scattered 355 nm excitation light (corresponding to the ~3650 cm^{-1} water O-H stretch) at ~405 nm [32] impaired the calculation of lifetimes from these wavelengths and were therefore excluded from analysis.

The measured average fluorescence lifetimes are affected by biochemical changes in tissue, notably the shift in the populations of the protein-bound and unbound forms of the metabolites NAD(P)H and FAD. To account for these changes, the fluorescence decays were also fit to a biexponential model, corresponding the unbound (β_1 and τ_1) and bound (β_2 and τ_2) populations (Fig. 5(A)-(C)). The necrotic tissue showed a significantly larger contribution and increase in lifetime from the bound fraction compared to healthy control and pre-necrotic brain tissue (Fig. 5(A) and 5(C), respectively). The biexponential analysis did not show any spectral signatures in pre-necrotic regions that were distinct from healthy controls. Minimal differences were present between the tissue types in the unbound fraction lifetime (Fig. 5(B)). Consistent trends across all tissue types included a decrease in lifetime with increasing wavelengths for both fractions and a decrease in the middle of the spectrum for the relative proportions of bound to unbound fractions.

Spectral fitting analysis was performed on the necrotic and healthy tissue to assess the relative contributions from commercially available NAD(P)H, FAD, and ECM/cholesterol (Fig. 5(D)-(E)). The tissue was well approximated using these fluorophores, as reflected through the fit coefficient of determinations (R^2) of 0.96 and 0.99 for healthy and necrotic tissue, respectively. The relative changes in spectral contributions for necrosis were -9% ECM/cholesterol, +5% NAD(P)H, and +4% FAD, relative to control healthy tissue. In summary, our results suggest there is a sizable change in the autofluorescence of necrotic tissue that is distinguishable from control and pre-necrotic tissue using p-TRFS.

3.2. In vitro studies with p-TRFS

To determine the relationship between biological mechanisms of necrotic cell death and the resulting changes in fluorescence signatures, we performed p-TRFS on the Fischer-rat-derived F98 cells that were subjected to different treatments that cause unprogrammed cell death, thus mimicking necrosis. F98 cells were treated with saponin–a surfactant that disrupts cell membranes, or sodium azide–an electron transport chain (ETC) inhibitor that alters the bound and unbound NAD(P)H content (Fig. 6). The treated and untreated groups showed spectral similarities, with minimal differences in peak position or contributions from FAD in the longer wavelengths (Fig. 6(A)). Significant differences were present in the average lifetimes of the treatment groups relative to the control, as observed in animal brain tissue. Saponin treatment caused an overall increase in lifetime, similar to the observation in necrosis *in vivo* (Fig. 4(A)-(B)), while sodium azide treatment caused a decrease in lifetime (Fig. 6(B)). Although all the cells, treated and control, had a blue-shifted peak compared to NAD(P)H, the spectra from the cells and NAD(P)H were otherwise quite similar. The spectra from cells had lower intensities at shorter wavelengths from 375-415 nm compared to that from tissue (Fig. 7(C)). The average lifetime values of cells was between that of normal and necrotic tissue types and showed a decrease in lifetime with increasing wavelengths, similar to *in vivo* observations (Fig. 6(D)).

3.3. Real-time tissue assessment with ms-TRFS

Brain tissue from necrotic and pre-necrotic animals and their corresponding normal controls were assessed using ms-TRFS (Fig. 1). The average lifetime and intensity measurements in necrotic tissue from the ms-TRFS system showed the same trends as p-TRFS: an increase in lifetime (effect size, ES > 0.8), redshift in normalized intensities (decrease in channel 1 (ES > 0.8), increase in channel 3 (ES > 1.2)), and increase in redox state (ES > 0.5) in comparison to

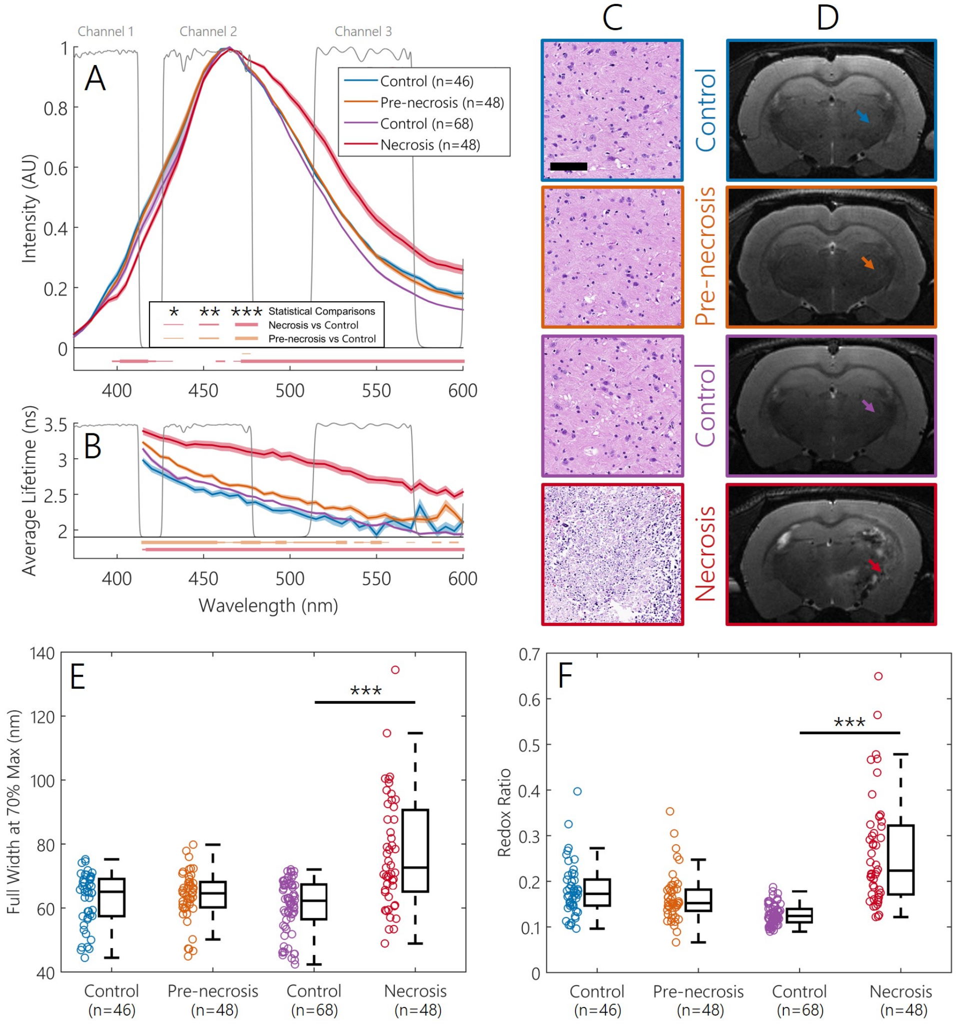

Fig. 4. p-TRFS measurements from pre-necrosis and necrosis rat brain tissue. Necrotic tissue demonstrates significantly longer lifetimes and increased redox state relative to control healthy tissues with p-TRFS measurements. (A-B) Normalized integrated intensity and average fluorescence lifetime; solid lines indicate the mean, with the shaded region showing mean ± SEM. The spectral integration windows for each of the three channels of the real-time ms-TRFS system are shown in gray. * $P < 0.05$, ** $P < 0.01$, *** $P < 0.001$ compared to corresponding control healthy tissue. (C) Representative H&E histology images at 10× magnification of the pre-necrotic and necrotic tissues along with their corresponding controls are presented. The scale bar is 100 μm. (D) Representative MRI images from each of the four tissue types; the approximate location of the corresponding histology shown in C is indicated with an arrow. (E) Full width at 70% of maximum values of the fluorescence intensity spectrum. (F) The redox ratio (fluorescence intensity of FAD to that of NAD(P)H) for the four tissue types. For E and F, *** ES < 0.001 compared to corresponding control healthy tissue. The number of samples indicated in the legends is the total number of spectra acquired for each tissue type.

the healthy control (Fig. 7(A)-(D)). The tissue regions with necrosis displayed heterogeneity

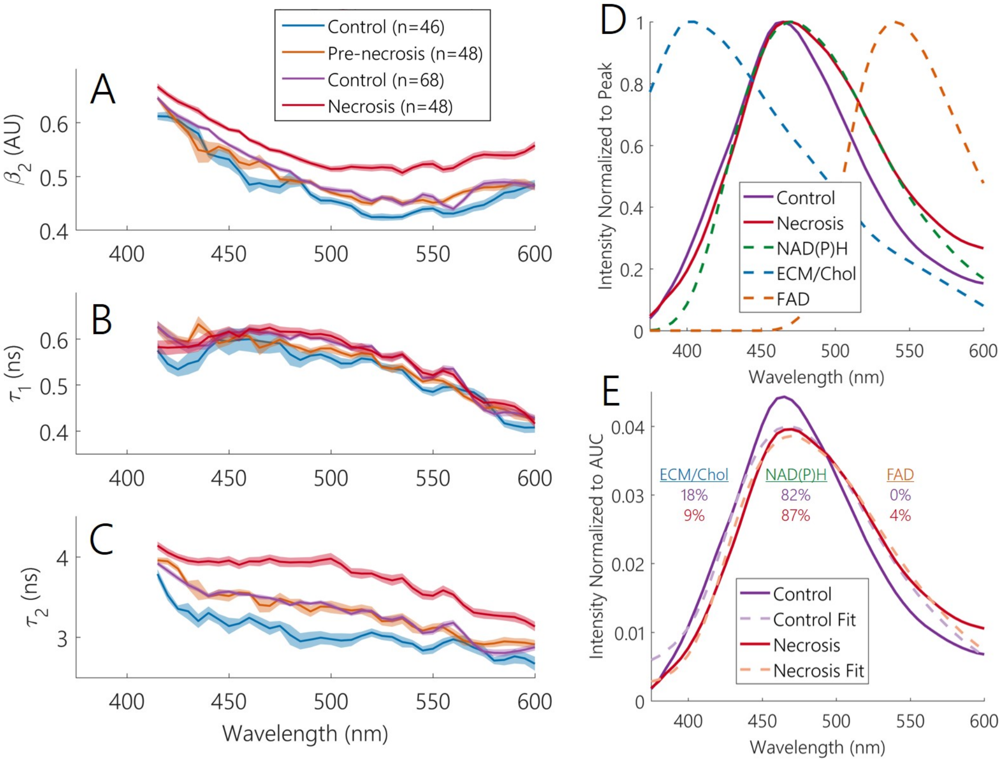

Fig. 5. Biexponential and spectral summation fitting analysis of p-TRFS data. Changes in the bound populations of NAD(P)H are the primary source of the increases in lifetimes observed. Biexponential fitting of the p-TRFS measurements for each of the tissue types; protein-bound fraction β_2 (A), fluorescence lifetime of unbound fraction τ_1 (B), and fluorescence lifetime of protein-bound fraction τ_2 (C). Spectral summation fitting analysis of the p-TRFS measurements. (D) The average measurements from healthy control and necrosis measurements, as well as NAD(P)H (combined as a single plot here), ECM/Cholesterol, and FAD intensity spectra normalized to peak value. (E) The control and necrosis spectra plotted along with their fit, normalized to the area under the curve (AUC). The coefficient of determination (R^2) for the fit of control and necrosis were 0.96 and 0.99, respectively.

in lifetimes, with prominent tails in the longer lifetime regions (Fig. 7(B)). Similar, albeit less pronounced, trends in lifetime and intensity were also observed in pre-necrotic tissue. An overall decrease in lifetime with increasing wavelengths was also observed in all tissue types (Fig. 7(B)).

One of the goals of this study was to evaluate how well we can discriminate necrotic regions from healthy brain using fluorescence lifetime signatures in real-time, clinically relevant conditions. To this end, a SVM-based supervised learning classifier was constructed using the ms-TRFS data. The performance of the classifier was assessed using a LOOCV protocol. Due to the lack of clinical consensus on the definition of pre-necrosis, only necrotic and healthy tissue were included in this analysis. In addition, for methodological verification, similar classifiers were built and validated using the p-TRFS data and p-TRFS data converted to ms-TRFS data (spectral bands). Finally, a detailed analysis was performed to assess if aging affects healthy brain tissue, in both the treated and control groups (see proceeding section for details). The analysis showed minimal effects of aging on spectral changes, within the context of individual animal differences and changes due to disease, and therefore, all the healthy tissue was grouped together in the

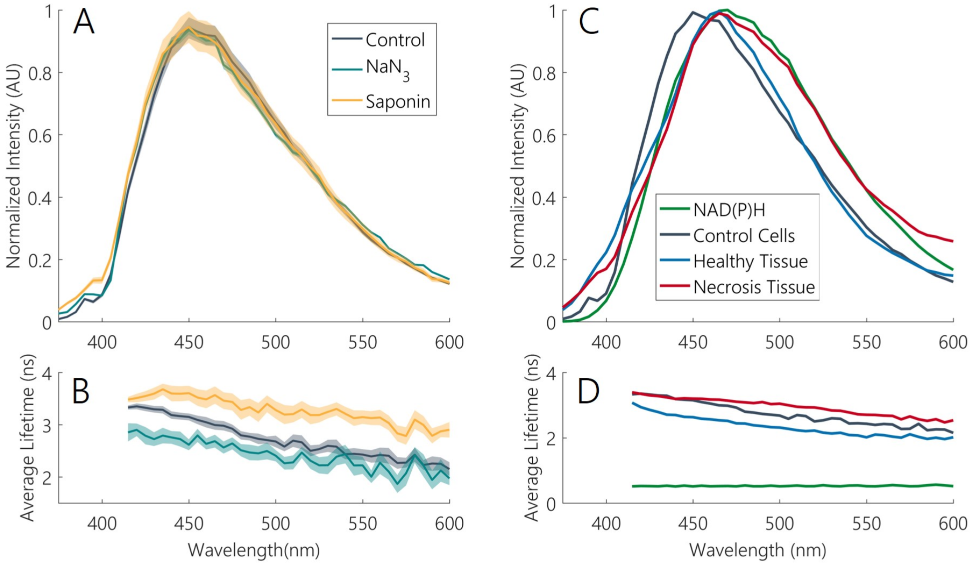

Fig. 6. In vitro cell culture studies using p-TRFS demonstrate similar trends to those found in vivo. The effects of the cellular membrane disrupter, saponin, and the cytochrome oxidase inhibitor, sodium azide (NaN_3), on normalized fluorescence intensity (A) and average lifetime (B) of F98 cells suspended in PBS. Solid lines indicate the mean and shaded regions showing mean ± SEM. To demonstrate the relative spectral contributions from NAD(P)H and the cells themselves, these spectra are plotted along with the two primary tissue types; normalized fluorescence intensity (C) and average lifetime (D). Note the spectrally flat lifetime of the pure fluorophore NAD(P)H solution relative to the spectrally changing cell and tissue lifetimes.

classifier (Fig. 8). Results from the LOOCV to detect the necrotic from healthy control tissues are shown in Table 1. Best performance was seen in the p-TRFS measurements (94% sensitivity and 97% specificity). Similar performance was observed in ms-TRFS and p-TRFS converted to ms-TRFS data (86/94% sensitivity and 93/100% specificity, respectively). All techniques reliably discriminated necrotic tissue from healthy brain tissue. The clinical necessity for rapid tissue assessment in combination with high accuracy in diagnosis makes ms-TRFS the technique that is best suited for clinical translation.

3.4. *Effect of animal age: control and healthy tissue comparisons*

Due to the nature of necrosis development, the pre-necrosis and necrosis animals will be of varying ages (~24 and ~31 weeks, respectively). To assess whether animal age influenced the fluorescence spectra, the non-irradiated tissues from the pre-necrosis and necrosis control groups were compared (Fig. 8(A)). Comparisons were performed for a variety of pathologically healthy and/or untreated tissues of interest. For these comparisons, only the channel 2 parameters from ms-TRFS measurements and redox ratio are plotted, as these parameters generally showed the largest differences between the tissue types and are also where the peak fluorescence occurs. Channels 1 and 3 displayed similar trends between the different tissue types and can be found in Table 2. The primary difference was a 0.1 ns decrease in lifetime of the pre-necrotic control tissue relative to the necrotic control tissues. Although no significant change in intensity or redox ratio was observed, the redox ratio had a noticeably broader distribution. To assess if any differences were present between left and right hemispheres, these tissues from the non-irradiated

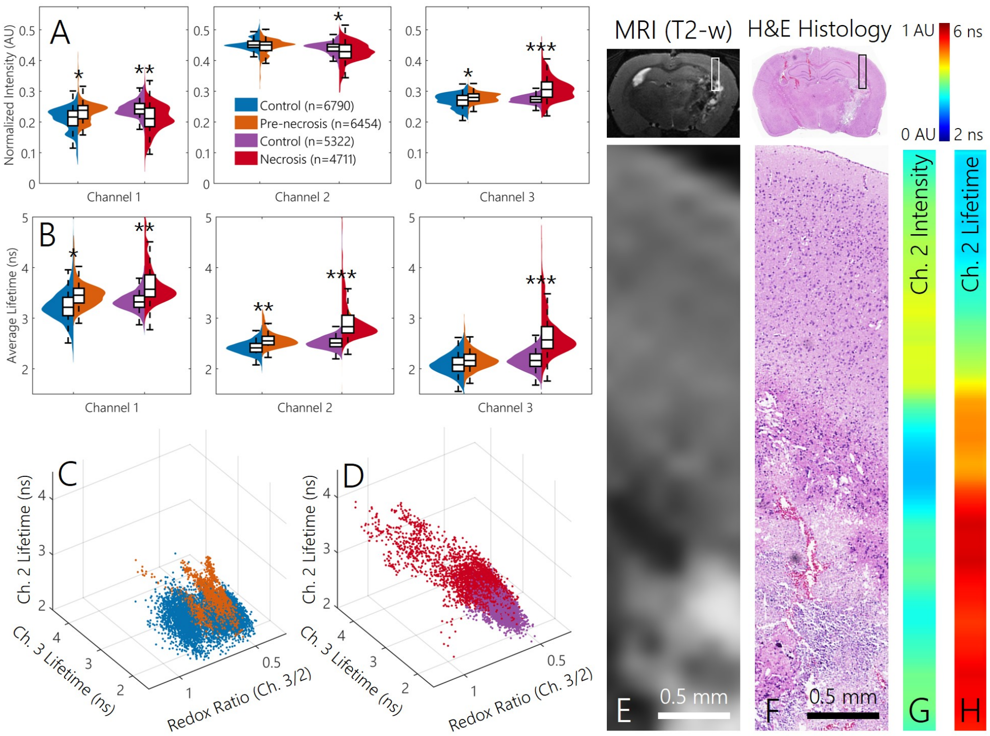

Fig. 7. Real-time tissue assessment from ms-TRFS system demonstrate similar tends as p-TRFS for pre-necrotic and necrotic tissues. (A-B) Normalized fluorescence intensity and average lifetime from the ms-TRFS channels (channel 1: 370-410 nm, channel 2: 456-484 nm, channel 3: 515-565 nm) comparing the four tissue types. (C-D) Three-dimensional visualization of the three most discriminating ms-TRFS parameters. Representative needle track in interrogated brain region with necrosis (4.0×0.9 mm^2 field of view) shows heterogeneity in regions with necrosis. T2-weighted MRI scan (E), corresponding H&E stained histology at 2× magnification (F), corresponding channel 2 fluorescence normalized intensity (G) and average lifetime (H). * ES > 0.5, ** ES > 0.8, and *** ES > 1.2 compared to corresponding control healthy tissue.

control groups were compared independently (Fig. 8(B)-(C)). Differences between the left and right non-irradiated healthy tissue from the pre-necrosis and necrosis control groups, across all fluorescence parameters, were less than 1%. This suggests that changes observed in the necrotic and pre-necrotic tissues were not due to differences in the brain hemisphere.

A final comparison assessed the irradiated tissue adjacent to where necrosis formed, but remained pathologically healthy according to histology and MRI. This tissue was compared to the non-irradiated-healthy tissues of the contralateral untreated hemisphere from the same animal, as well as the healthy tissue from the non-irradiated necrosis control group (Fig. 8(D)). Although no significant differences in intensity were present between the tissues types, there was a small but statistically significant increase in lifetime of the tissue adjacent to necrotic relative to control tissues. The redox ratio was found to be lower than the control tissues, albeit with a slightly broader distribution. Differences between the contralateral and controls tissues were not significant for any parameter.

Table 1. An SVM classifier was constructed to separate necrotic from healthy control tissue using fluorescence lifetime parameters and was validated using a LOOCV protocol. Sensitivity (SN) of necrosis identification, specificity (SP) of identification of healthy tissue, positive predictive value (PPV), and negative predictive value (NPV) for the two instrumentation systems, ms-TRFS and p-TRFS, are shown. As a methodological validation, the classification performance was also evaluated for the p-TRFS data converted to the three channels of the ms-TRFS system.

System	Data Points	SN (%)	SP(%)	PPV (%)	NPV (%)
ms-TRFS	Healthy (n = 5,322) Necrosis (n = 4,711)	86	93	90	88
p-TRFS	Healthy (n = 68) Necrosis (n = 48)	94	97	96	96
p-TRFS converted to ms-TRFS	Healthy (n = 68) Necrosis (n = 48)	94	100	100	96

3.5. Stratified histological necrosis grading

Radiation-induced necrosis is known to be very heterogeneous [8], with a variety of histological features present as the disease progresses spatiotemporally [31]. Although MRI scans provide improved coregistration compared to histology, they do not provide either the spatial resolution or the contrast to assess the heterogeneities and uncertain borders found within the necrosis. To assess whether the higher spatial sampling obtained using ms-TRFS can identify these finer features, a stratified histological grading system based on a previously published method was employed with consensus among two researchers [31]. The features of the three grades was as follows (Fig. 9(A)-(D) shows histology images representative of stratified histology classes): Grade I contained micro-hemorrhages and inflammatory cells, Grade II contained tissue loss and vascular hyalinization, and Grade III contained extensive tissue loss, edema, and fibrinoid vascular necrosis. Since H&E histologic sections were necessary to classify the tissue for this method, only regions with needle tracks definitively present in the histology sections were included in the analysis. The three grades of necrosis all followed the trends observed with the singular grading of necrosis; primarily a redshift of normalized intensity, increase in lifetime, and increase in redox ratio (Fig. 9(E)-(G)). As the necrosis progressed from Grade I to Grade III, the trends were approximately monotonic, such that Grade III (approximating the center of necrosis) had the highest lifetimes and redox ratios.

4. Discussion

4.1. Mechanisms of endogenous fluorescence contrast: normal brain versus necrotic tissue

The current study demonstrates that necrotic tissue has three primary fluorescence features distinguishing it from healthy brain tissue: an increase in average lifetime at all wavelengths (Fig. 4(B)), an increased redox ratio (Fig. 4(F)), both attributed to metabolic changes in tissue, and a decrease in intensity at 400-420 nm, attributed to changes in tissue ECM and morphology (Fig. 4(A)). The regions of necrosis are highly heterogeneous and contain different combinations of debris, viable but hypoxic native cells, and inflammatory cells. The observed increase in redox ratio in regions with necrosis, are indicative of an increased presence of FAD compared to NAD(P)H (Fig. 5(E)) and thus, a metabolic shift towards oxidative state in necrotic tissue. This finding is somewhat counterintuitive given that the disrupted blood supply in necrotic areas may lead to hypoxia [33]. However, the increased presence of FAD relative to NAD(P)H may be

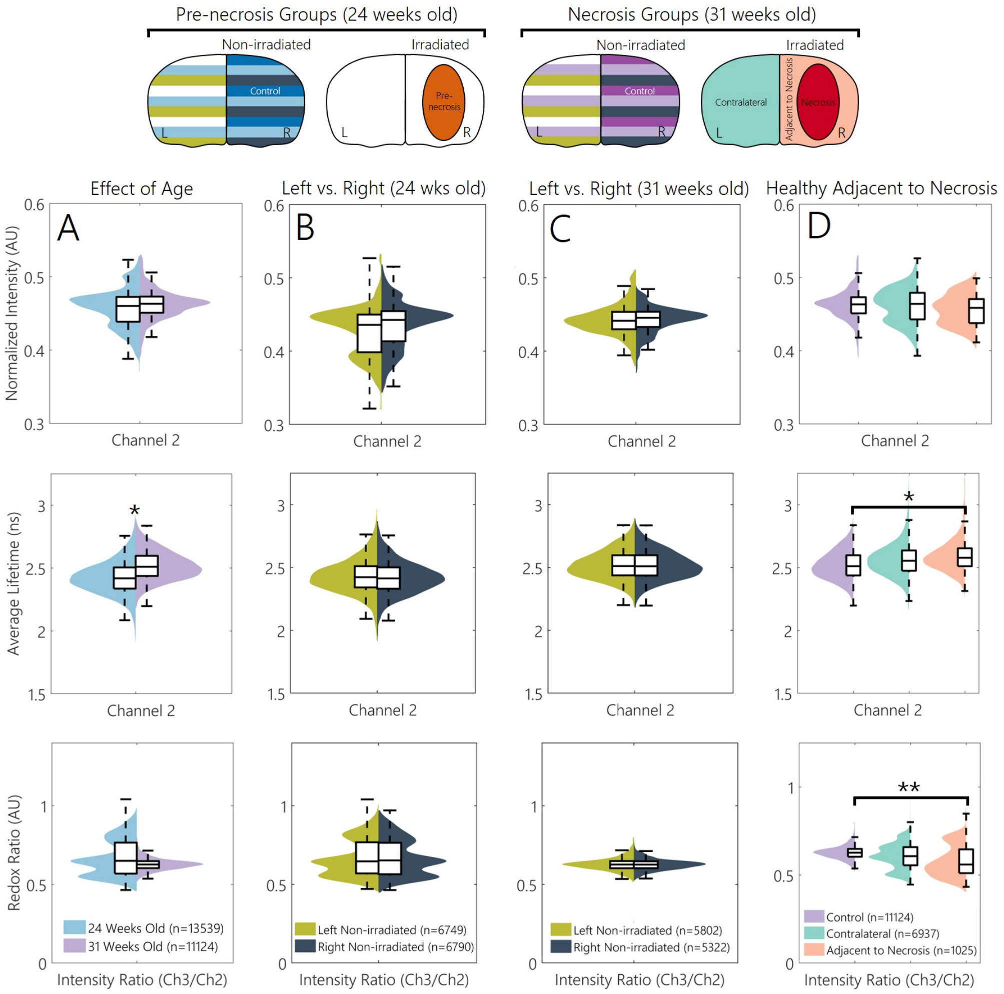

Fig. 8. Real-time ms-TRFS measurements detect subtle changes in the age of healthy non-irradiated control animals, as well as healthy tissues in irradiated animals. (A) Comparing the healthy tissues from both hemispheres between the two non-irradiated control groups (pre-necrosis controls at ~24 weeks old, necrosis controls at ~31 weeks old). (B-C) Differences between the left and right hemispheres for the pre-necrosis controls and necrosis controls. (D) The tissue which received a radiation dose but did not form into necrosis (Adjacent to Necrosis) were also compared to the healthy tissue from the contralateral hemisphere (Contralateral) of irradiated necrosis animals as well as the healthy tissue of the necrosis control animals (Control). Most significant ms-TRFS parameters are plotted for each case; channel 2 normalized fluorescence intensity (top) and average lifetime (middle), and redox ratio (bottom). Color coded diagrams of each animal group's brain at the top inset indicate where the different compared tissues were from; note that all left hemispheres were not irradiated. * ES > 0.5 and ** ES > 0.8.

explained by the fact that the cellular debris are more likely to be oxidized than reduced when in the extracellular environment.

Biexponential fluorescence decay analysis demonstrated that the increase in average lifetime was primarily due to an increase in the long decay component, τ_2 (Fig. 5(C)), as well as an increased contribution from this component, β_2 (Fig. 5(A)). The increase in β_2 reflects an increase

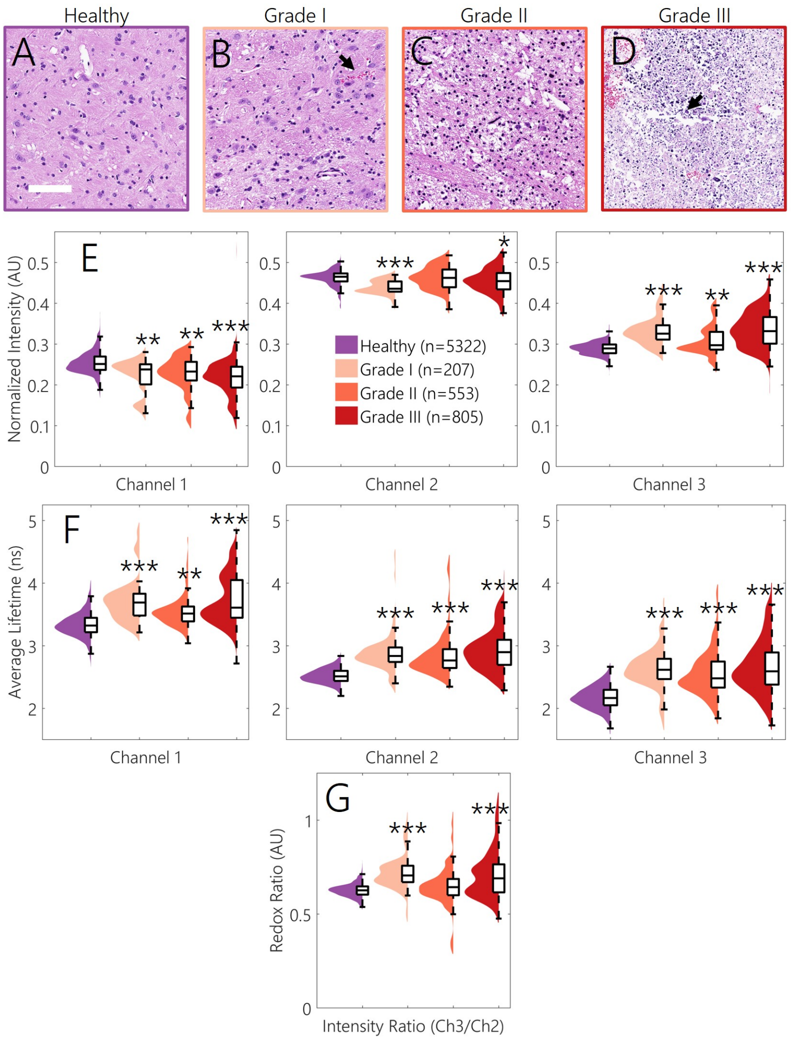

Fig. 9. Real-time ms-TRFS discriminates between healthy and stratified histological grades of necrosis. Representative histology images of the different grades of brain necrosis; all tissue is shown at 10× magnification and stained with H&E. Grade 0: normal healthy (A); Grade I: micro-hemorrhages present (B); Grade II: inflammation and minor tissue loss (C); Grade III: edema, extensive tissue loss, and calcifications (D). Histological images taken from the lateral thalamus region of the brain, roughly corresponding to the peak radiation dose and focalization of necrosis formation. Scale bar shown is 100 μm. Comparison between control healthy, Grade I, Grade II, and Grade III necrotic tissue types for integrated intensities (E), average lifetimes (F), and redox ratio (G). * ES > 0.5, ** ES > 0.8, and *** ES > 1.2 compared to control healthy tissue.

in the proportion of the protein-bound NAD(P)H relative to the unbound fraction. This is likely caused by an increased build-up of bound NAD(P)H in the tricarboxylic acid cycle–via restriction of the ETC–due to the hypoxic state of the necrosis. The increase in τ_2 could be caused by a shift in the enzyme populations to which NAD(P)H is bound as a result of the presence of native hypoxic cells [34, 35]. This change can be also be attributed to an increase in the amount of bound NADPH relative to bound NADH [36] due to the recruitment of catabolically active

Table 2. Summary of the ms-TRFS measurements comparing the different tissues types from all studied groups; mean ± SD are shown.

Animal Group–Tissue Type	Intensity (AU) Ch. 1	Intensity (AU) Ch. 2	Intensity (AU) Ch. 3	Lifetime (ns) Ch. 1	Lifetime (ns) Ch. 2	Lifetime (ns) Ch. 3	Redox Ratio Ch. 3/2
Pre-necrosis Control–Right Healthy	0.22 ± 0.04	0.46 ± 0.03	0.31 ± 0.04	3.24 ± 0.35	2.42 ± 0.14	2.09 ± 0.20	0.65 ± 0.13
Pre-necrosis–Right Irradiated Pre-necrosis	0.23 ± 0.04	0.47 ± 0.03	0.31 ± 0.03	3.30 ± 0.29	2.50 ± 0.16	2.10 ± 0.19	0.65 ± 0.06
Necrosis Control–Right Healthy	0.25 ± 0.03	0.46 ± 0.02	0.29 ± 0.02	3.33 ± 0.19	2.52 ± 0.12	2.17 ± 0.18	0.63 ± 0.04
Necrosis–Right Irradiated Necrosis	0.24 ± 0.08	0.45 ± 0.04	0.32 ± 0.06	3.70 ± 0.45	2.96 ± 0.44	2.68 ± 0.45	0.65 ± 0.20
Pre-necrosis Control–Healthy (24 wks)	0.22 ± 0.03	0.46 ± 0.03	0.31 ± 0.04	3.26 ± 0.35	2.42 ± 0.14	2.09 ± 0.20	0.67 ± 0.11
Necrosis Control–Healthy (31 wks)	0.25 ± 0.03	0.46 ± 0.02	0.29 ± 0.02	3.36 ± 0.21	2.52 ± 0.12	2.17 ± 0.18	0.63 ± 0.04
Pre-necrosis Control–Left Healthy	0.23 ± 0.03	0.45 ± 0.03	0.31 ± 0.04	3.28 ± 0.36	2.43 ± 0.14	2.10 ± 0.20	0.65 ± 0.13
Pre-necrosis Control–Right Healthy	0.22 ± 0.04	0.46 ± 0.03	0.31 ± 0.04	3.24 ± 0.35	2.42 ± 0.14	2.09 ± 0.20	0.65 ± 0.13
Necrosis Control–Left Healthy	0.25 ± 0.03	0.46 ± 0.02	0.29 ± 0.02	3.39 ± 0.21	2.52 ± 0.12	2.17 ± 0.18	0.63 ± 0.04
Necrosis Control–Right Healthy	0.25 ± 0.03	0.46 ± 0.02	0.29 ± 0.02	3.33 ± 0.19	2.52 ± 0.12	2.17 ± 0.18	0.63 ± 0.04
Necrosis Control–Right Healthy	0.25 ± 0.03	0.46 ± 0.02	0.29 ± 0.02	3.33 ± 0.19	2.52 ± 0.12	2.17 ± 0.18	0.63 ± 0.04
Necrosis–Left Non-irradiated Healthy	0.24 ± 0.06	0.46 ± 0.02	0.29 ± 0.04	3.43 ± 0.29	2.56 ± 0.15	2.19 ± 0.20	0.56 ± 0.14
Necrosis–Right Irradiated Healthy	0.24 ± 0.05	0.46 ± 0.02	0.29 ± 0.03	3.41 ± 0.27	2.59 ± 0.13	2.21 ± 0.21	0.48 ± 0.18
Necrosis Control–Right Healthy	0.25 ± 0.03	0.46 ± 0.02	0.29 ± 0.02	3.33 ± 0.19	2.52 ± 0.12	2.17 ± 0.18	0.63 ± 0.04
Necrosis–Right Irradiated Grade I	0.22 ± 0.04	0.44 ± 0.02	0.33 ± 0.03	3.71 ± 0.33	2.88 ± 0.31	2.63 ± 0.31	0.72 ± 0.09
Necrosis–Right Irradiated Grade II	0.23 ± 0.04	0.46 ± 0.03	0.31 ± 0.04	3.54 ± 0.24	2.86 ± 0.36	2.56 ± 0.36	0.65 ± 0.11
Necrosis–Right Irradiated Grade III	0.22 ± 0.04	0.45 ± 0.03	0.33 ± 0.04	3.73 ± 0.38	2.93 ± 0.33	2.66 ± 0.42	0.71 ± 0.12

inflammatory cells [37]. While identification of the precise enzymatic sources of the observed shifts in metabolite populations is challenging [38], fluorescence lifetime assessment is an easily accessible technique to evaluate these shifts.

The decrease in fluorescence intensity at 400-420 nm can be attributed to a loss of the ECM (Fig. 5(E)) and structural molecules in the tissue. Several of these molecules present in the brain–such as aggrecan [25], chondroitin sulfate [26], and cholesterol [27]–are known to have a peak fluorescence emission within this wavelength region (Fig. 5(D)). The loss of the ECM and structural molecules is a well-known feature of necrosis and is demonstrated by the widespread tissue loss that was observed in the histological analysis of the tissues (Fig. 4(C) and Fig. 9(C)-(D)). The *in vitro* cell studies–for which no ECM is present–further support this finding, as relative to the healthy tissues, there was minimal fluorescence signal measured in this spectral region from the cells (Fig. 6(C)).

A leading mechanistic hypothesis for the development of radiation-induced necrosis postulates that the first step is a change in the endothelial cells, which are responsible for the vascular supply in tissue [33]. Although radiation may cause significant metabolic changes to the endothelial cells, the relative abundance of these cells in the brain is very small in comparison to neuronal and glial cells, and thus unlikely to influence bulk tissue metabolism. The lack of significant changes in tissue metabolism, measured with fluorescence lifetime, in pre-necrotic tissue (Fig. 4(A)-(B) and Fig. 7(A)-(C)) support this hypothesis. Previous MRI studies have found that the breakdown of the blood-brain-barrier for the radiation dose used in this study (60 Gy) begins to occur at 18 weeks, which is 1-2 weeks after the pre-necrosis animals in this study were assessed [19]. This supports the lack of hypoxia-related fluorescence spectral changes in pre-necrotic tissue.

A variety of trends were present in the measured fluorescence lifetimes of all tissues types, irrespective of radiation treatment. The most evident change was a consistent, monotonic decrease in lifetime with wavelength which was present in both the animal (Fig. 5(B)) and *in vitro* studies (Fig. 6(B)). This has also been observed in previous studies in human brain tissue [16, 18]. At longer wavelengths (greater than ~475 nm) this trend can be attributed to contributions from FAD, which has an average lifetime that is three times shorter than that of NAD(P)H when measured in live healthy tissue [34]. For the wavelengths below the FAD emission spectra (Fig. 5(D)), the trends can potentially be explained by the changes in fluorescence emission when NAD(P)H is bound to enzymes. The binding of NAD(P)H to enzymes causes a blue-shift in spectral emission [39] and an increase in both lifetime and quantum yield [40]. These changes are caused by how tightly the enzymes hold NAD(P)H rigidly in the stretched conformation and therefore reducing the non-radiative relaxation rate [41]. There is a wide variety of enzymes that bind to NAD(P)H–each with different binding characteristics and therefore varying effects on fluorescence spectra. At blue-shifted wavelengths, there is a greater likelihood of increased spectral contributions from the more tightly bound NAD(P)H causing longer lifetimes and quantum yields and thus, an increase in average lifetime at these wavelengths. This hypothesis is supported in the biexponential analysis of p-TRFS data in the animal model, where the contribution and lifetime from the bound fraction (β_2 and τ_2) both steadily increase, moving from 530 nm to 415 nm, while the lifetime of the unbound fraction (τ_1) remains relatively constant (Fig. 5(A)-(C)). At wavelengths beyond ~530 nm both τ_1 and τ_2 continue to decrease, again due to the increased contributions from FAD, which has been previously measured to have lower τ_1 and τ_2 than NAD(P)H [34].

The results from our *in vitro* cell studies suggest that intracellular contributions are largely responsible for the fluorescence changes observed in tissue. Both the emission spectra and average lifetimes of the cells were very similar to those of the tissue, with the primary difference being the reduced fluorescence around 375-400 nm, attributable to the lack of ECM and structural molecules *in vitro* (Fig. 6(C)-(D)). This indicates that most of the observed changes in fluorescence of the tissue originate from intracellular sources and agrees well with results from the spectral contribution analysis (Fig. 5(E)). Although the saponin or sodium azide treatment did not generate any changes in the emission spectra, supporting the observation in tissue studies that new proteins with fluorescent signatures were not generated during disease development, significant changes in lifetime were present (Fig. 6(A)-(B)). Saponin generated an externally-mediated, less-structured cell death similar to necrosis, and caused an increase in lifetime across all wavelengths, similar to observations in tissue (Fig. 6). In contrast, as expected, the cells treated with sodium azide, which causes an internally-mediated cell death by inhibiting the ETC and generating more unbound NADH in the process, resulted in a shorter average lifetime due to the additional unbound NADH generated. These results provide further evidence that the TRFS technique is sensitive to intracellular metabolism and capable of detecting different mechanisms of cell death.

4.2. *Real-time metabolic spectroscopy of a brain with ms-TRFS*

The fluorescence trends in lifetime and intensity measured in live brain using the ms-TRFS (Fig. 7(A)-(D) and Fig. 2) were consistent with the trends from the p-TRFS system. However, due to a faster signal acquisition mechanism that better supports clinical implementation, it has a much higher spatial sampling than the p-TRFS system. Moreover, the ms-TRFS measurements in necrotic tissue and healthy brain regions correlate very well with both histology and MRI scans (Fig. 7(E)-(H)) thus demonstrating that this approach is a viable option for real-time necrotic tissue detection during MRI-guided stereotaxic biopsy procedure. The ms-TRFS instrumentation setup provided significantly improved spatial resolution (100 µm lateral, ~50 µm axial) and specificity over current clinical MRI scanners and other available imaging modalities (Fig. 7(E)-(F)). While the spatial resolution of the current ms-TRFS system does not approach that of histology, the fluorescence signatures correlate well with the stratified histology grading analysis of necrotic regions (Fig. 9). This is of key importance for future translation to the clinical setting where the observed spatial variability of the necrosis will need to be accurately assessed. The automated classification of necrotic and healthy tissue demonstrated that measurements from both the p-TRFS and ms-TRFS systems can identify the necrotic tissues with good performance (Table 1), though p-TRFS showed superior performance. This disparity, however, can likely be overcome my modifying the spectral bands of the ms-TRFS system. More specifically, the channel 3 band could be red-shift to increase the contributions of FAD to it, and the channel 2 band could be blue-shifted to increase the contributions to NADH to it.

The ms-TRFS measurements comparing the left and right hemispheres of the non-irradiated control groups were consistent, with less than 1% difference between the two sides for all parameters (Table 2). The main physical difference between the control groups for the necrosis and pre-necrosis animals was age. In comparing these groups, we found that in addition to small changes in lifetime, a significantly larger variability was present in the redox ratio of the pre-necrosis control group (~24 weeks old) (Fig. 4(A)). Further analysis showed that the increased variability was due to inter-animal differences as opposed to consistent changes across the control groups. The older and heavier animals in the necrosis control group (~31 weeks old) were perhaps less susceptible to fluctuations in metabolism caused by anesthesia or the warming bed during surgery. Future studies would benefit from having the animal ventilated and using feedback from blood gas monitoring to ensure consistent tissue oxygenation throughout the entire procedure.

Changes in fluorescence signatures were detected in the irradiated brain hemisphere in regions surrounding necrosis that were designated as healthy per histology and MRI analysis (Fig. 7(D)). These spectral changes were similar to trends observed in pre-necrotic regions: small increase in average lifetime, and elevated redox ratio (Fig. 7(D)). Since the necrosis animals were assessed at the peak of necrosis formation, with blood brain barrier healing expected to occur within 1-2 weeks after the optical interrogation time point [19], we believe it is unlikely that these regions with hallmarks of pre-necrosis will ever progress to necrosis. We hypothesize that these tissue changes are a result of an inflammatory response. The observed spectral changes were limited to only the treated hemisphere, with the contralateral side not showing any significant differences. For future 60-Gy dose plan LINAC studies, we believe the tissue from the left non-irradiated hemisphere could serve as adequate control, without the need for non-irradiated animals.

A variety of challenges exist for comparing our results to previous fluorescence lifetime studies on brain tissue, notably those which measured tumors. Necrotic tissue is a mixture of intact cells and cellular debris, unlike intact tissue in which previous studies have been performed. The ECM changes in necrosis affect the transport of free extracellular NADH across the plasma membrane, and thus alters the proportion of protein-bound and unbound NADH fractions and consequently, measured lifetimes [37]. Previous studies performing analysis of FAD have generally used a second excitation wavelength. While this will not have any direct affect on the lifetimes observed (due to lifetime being a state function [23]), the suboptimal excitation of FAD most likely will affect the intensity and therefor the magnitude of the changes in redox ratio. Another challenge for making comparisons with existing literature arises from methodological differences in fluorescence lifetime imaging. Two-photon excitations setups are most commonly used for brain studies, and significant differences have been reported in both fluorophore behavior and intact tissue spectra when comparing two-photon excitation versus single photon excitation setups [42]. Compared to the limited other *in vivo* murine studies, our average lifetimes for healthy control tissues were approximately 1.2 ns higher than those reported [38, 43]. These differences likely stem from a variety of factors, including anesthetics used, age and breed of the rodents, lifetime fitting software, and the large difference in anatomical regions interrogated. However, hypoxic brain tissue has been assessed previously and a lower lifetime has been reported due to an increase in contribution from the unbound NAD(P)H fraction [43]. In addition, previous *in vivo* studies have found significant changes in average lifetime and contribution from protein-bound NAD(P)H fractions as a function of disease [38, 44]. Our observations of spectral changes in necrotic brain tissue compares well with the limited existing and parallel literature in fluorescence lifetime imaging [45], within the context of hypoxia changes and ETC changes driving the progression of necrosis.

5. Conclusion

This study demonstrates in a live rat model the ability of TRFS to differentiate radiation-induced brain necrosis from normal brain based on the tissue's intrinsic molecular contrast. Concurrent *in vitro* studies and analysis elucidated the endogenous fluorescence sources of contrast observed.

Compared to healthy brain tissue, necrotic tissue displayed increases of 27% in average lifetime and 108% in redox ratio. Measurements of the irradiated tissue just prior to pathological necrosis formation (i.e. pre-necrosis) showed minimal differences relative to the healthy tissue, suggesting that the endothelial cells of the vasculature–rather than the neuronal or glial cells–are the initial causes for late-onset radiation-induced necrosis. Analysis of the TRFS data from both live brain tissue and *in vitro* cell studies demonstrated that the intracellular fluorophores, NAD(P)H and FAD, were the primary biochemical sources of signal, and the differences observed in the necrotic tissue were primarily due to shifts in the populations of enzymes binding NAD(P)H.

This study also demonstrates a rapid tissue diagnostic ms-TRFS technique suitable to implementation in the clinical setting for in situ real-time delineation of necrotic regions from normal brain. We show that a supervised classification algorithm using parameters derived from the ms-TRFS measurements conducted via a needle progressively advanced into live brain allows for differentiation of necrotic tissue from healthy brain with a sensitivity of 94% and specificity of 97%. These results demonstrate the potential of this technique for real-time metabolic spectroscopy of brain tissue during surgical- or stereotaxic-biopsy procedures. Consequently, this approach has far-reaching implications in surgical decision making and MRI guided biopsy.

Funding

National Institutes of Health (NIH) (R21CA178578).

Acknowledgments

This work was supported by the UC Davis Comprehensive Cancer Center's Brain Malignancies Innovation Group. We thank K. Kim for assistance with statistical analysis, J. Garbow (Washington University) for useful discussions and advice with the MRI scans, P. Magee for help with rodent anesthesia for irradiation procedures, J. Perks for generating radiation dose plan, J. Bec and D. Ma for help with the TRFS instrumentation setup, A. Valenzuela for assistance with histology, and V. Srinivasan, M. Klich, J. Phipps, and B. Sherlock for help with manuscript editing.

Disclosures

The authors declare that there are no conflicts of interest related to this article.